Design of a Payload Pointing Control System for Tracking Moving Objects

Hari B. Hablani
Rockwell International, Seal Beach, California

A payload pointing control system for tracking an arbitrarily moving object is presented. The angular position, rate, and acceleration commands are developed in order for a two-degree-of-freedom telescope to track the object. The bandwidth of the control system is determined on the basis of the Fourier spectra of the rate commands and rate error specifications. The pointing control system operates in three modes: a linear rate mode for tracking, a linear position mode for settling, and a nonlinear position mode for coasting. The rate mode is a high bandwidth system (1.6 Hz), uses inertial rate commands, and consists of a double proportional-plus-integral (PI) controller. The position mode comprises the closed-loop rate mode and an additional PI controller; it works on relative position commands and has low bandwidth (0.32 Hz). The steady-state rate and position errors involve spectral density of the commands and the transfer functions of the controllers. The analysis is illustrated for a landmark observation with a near-Earth spacecraft. The settling times and steady-state errors based on single-axis and dominant pole approximations are compared with those from an extensive nonlinear digital simulation.

I. Introduction

THIS paper presents a precision pointing control system for landmark observations or for tracking any other moving object. The angular position, rate, and acceleration commands for tracking an arbitrarily moving object with a telescope (also called payload) hard-mounted on a three-axis stabilized base body are presented in Sec. II. These commands can be specialized for situations such as landmark observation or tracking a ballistic, orbiting, or celestial object. The position commands are derived relative to the base body that rotates once per orbit. Both relative and inertial, rate, and acceleration commands are formulated. A subset of these commands was derived earlier by Jerkovsky.[1] Burdick et al.[2] have also devised position and rate commands relative to the base body for tracking a celestial object.

The methodology to design a pointing control system depends on the target kinematics and the surroundings of the pointing control system. For example, in the case of Galileo spacecraft, the design is heavily influenced by a flexible thin shell structure on which the scan platform is mounted. To minimize the structural vibrations, a smooth feed-forward torque and smooth rate and position commands are used (Man and Breckenridge[3]). To perform a raster, a racetrack, or a strip scan on the celestial sphere with the Infrared Astronomical Satellite, Zwartbol et al.,[4] experimented with a dual-mode control policy comprising a time-optimal control and a linear proportional-plus-integral-plus-derivative (PID) control. Hughes[5] discusses a methodology for designing a PID pointing control system for Space Station gimbaled payloads that may receive a wide spectrum of jitter from a significantly deformable keel base; the study, however, is restricted to inertially stationary targets only.

The methodology adopted in Sec. III of this paper for tracking a moving object is this (Masten[6], Sirlin and Bell[7]): develop a stabilization subsystem to minimize inertial jitter and then design a track subsystem to control the overall orientation. Along with the single-axis assumption, the techniques of pole placement, dominant pole approximation, root locus, and steady-state error analysis are utilized to synthesize the controller. In Sec. IV the steady-state error (or jitter) in tracking is evaluated by expressing the position command as the sum of a step command, a ramp command, a parabolic command, and sine and cosine harmonic series. The rate command is expanded similarly. To determine the frequency spectra and spectral densities, the commands are modeled in two ways: as periodic commands that exist for the interval $-\infty \leq t \leq \infty$, and so their spectra are discrete, and as aperiodic commands that exist for a finite interval, and so their spectra are continuous. Numerical results based on the analysis in Sec. II–Sec. IV are discussed in Sec. V.

II. Commands for Tracking an Arbitrarily Moving Target

To track a moving object, a telescope is articulated to an Earth-orbiting base body to which a solar array is also hinged

Dr. Hari B. Hablani received his M.E. and Ph.D. in Aeronautical Engineering in 1978 from the Indian Institute of Science, Bangalore, India. He was then a post-doctoral fellow in the Department of Aeronautics and Astronautics at Purdue University, West Lafayette, Indiana, for two years, where he had an opportunity to work with Prof. Robert E. Skelton, and Prof. Peter C. Hughes from the Institute for Aerospace Studies, University of Toronto, Downsview, Ontario, Canada. After this, he was a NASA National Research Council Associate for two years at Johnson Space Center, Houston, Texas. Since 1982 he has been with the Guidance and Control Group, Rockwell International, Satellite Systems Division, Seal Beach, California. His field of specialization is the dynamics and control of multibody flexible spacecraft.

Received June 19, 1987; revision received Oct. 21, 1987.

(see Fig. 1). The three coordinate frames shown in Fig. 1 for deriving the commands are as follows: $\boldsymbol{c}_1, \boldsymbol{c}_2, \boldsymbol{c}_3$ constitute a dextral triad of unit vectors that rotates once per orbit about $\boldsymbol{c}_2$ with a clockwise angular speed of ω_0; $\boldsymbol{c}_1$ points along the orbital velocity of the spacecraft, and $\boldsymbol{c}_3$ is along the local vertical and points toward the earth; $\boldsymbol{b}_1, \boldsymbol{b}_2, \boldsymbol{b}_3$ constitute a base-body-attached unit vector triad. Furthermore, $\boldsymbol{p}_1, \boldsymbol{p}_2, \boldsymbol{p}_3$ make up a payload-attached unit vector triad; the payload rotates relative to the base body by an angle θ_{p1} about the vector $\boldsymbol{b}_1$ and θ_{p2} about $\boldsymbol{p}_2$. Nominally, the three triads are parallel. V^* in Fig. 1 is the mass center of the three-body spacecraft. The geometry of the motion of the spacecraft and of the object to be tracked is shown in Fig. 2. The object may be a landmark on the Earth, a vessel on the ocean, or a ballistic missile, or it may be an object traversing a trajectory in space (as depicted in Fig. 2).

Position Commands

Let ℓ be the line-of-sight (LOS) vector from V^* to the target T (Fig. 2). To determine position commands, ℓ is set parallel to $\boldsymbol{p}_3$, i.e.,

$$\ell = \ell \boldsymbol{p}_3 \tag{1}$$

where $\ell = |\ell|$. This desired direction is obtained by commanding the payload to rotate by an angle θ_{p1c} about $\boldsymbol{b}_1$ and θ_{p2c} about $\boldsymbol{p}_2$ (the subscript c is for commanded angle). The vector $\boldsymbol{p}_3$ is then related to the triad $\boldsymbol{b}_1, \boldsymbol{b}_2, \boldsymbol{b}_3$, thus

$$\boldsymbol{p}_3 = s\theta_{p2c}\boldsymbol{b}_1 + c\theta_{p2c}(-\boldsymbol{b}_2 s\theta_{p1c} + \boldsymbol{b}_3 c\theta_{p1c}) \tag{2}$$

where $s(\cdot) = \sin(\cdot)$, and $c(\cdot) = \cos(\cdot)$. Because the trajectories of the spacecraft and the target are assumed to be known, the vector ℓ is also known and can be written in the triad $\boldsymbol{b}_1, \boldsymbol{b}_2, \boldsymbol{b}_3$ as

$$\ell = \ell \cdot \boldsymbol{b}_1 \boldsymbol{b}_1 + \ell \cdot \boldsymbol{b}_2 \boldsymbol{b}_2 + \ell \cdot \boldsymbol{b}_3 \boldsymbol{b}_3 \tag{3}$$

Substituting Eq. (2) in Eq. (1) and comparing it with Eq. (3), the following relative position commands are obtained [cf. Eqs. (4) and (5) of Burdick et al.[2] and Eqs. (2–5) of Jerkovsky[1]]:

$$\theta_{p1c} = \tan^{-1}[-(\ell \cdot \boldsymbol{b}_2)/(\ell \cdot \boldsymbol{b}_3)] \tag{4a}$$

$$\theta_{p2c} = \tan^{-1}[(\ell \cdot \boldsymbol{b}_1)c\theta_{p1c}/(\ell \cdot \boldsymbol{b}_3)] \tag{4b}$$

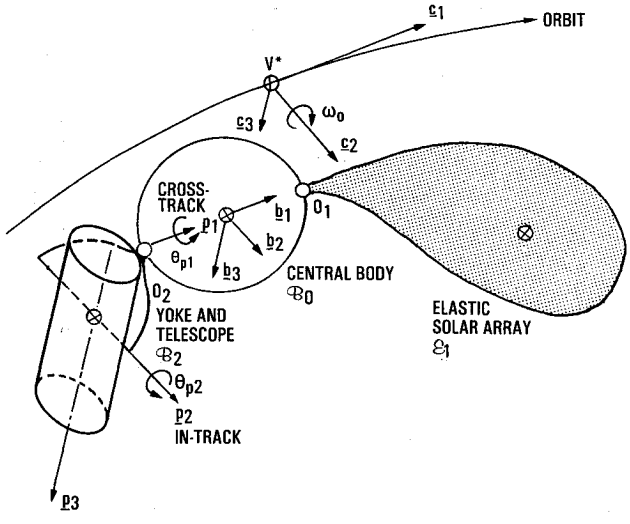

Fig. 1 Three-body precision pointing spacecraft.

Inertial and Relative Rate Commands

Let $\dot{\boldsymbol{r}}_T$ and $\dot{\boldsymbol{r}}_s$ be the known inertial velocities of the target and the spacecraft; then the inertial rate of change of the LOS vector, denoted $\dot{\ell}$, equals

$$\dot{\ell} = \dot{\boldsymbol{r}}_T - \dot{\boldsymbol{r}}_s \tag{5}$$

In the triad $\boldsymbol{p}_1, \boldsymbol{p}_2, \boldsymbol{p}_3$, the target has no rectilinear motion along the $\boldsymbol{p}_1$ and $\boldsymbol{p}_2$ axis, i.e.,

$$\dot{\ell} = (0)\boldsymbol{p}_1 + (0)\boldsymbol{p}_2 + \dot{\ell}\boldsymbol{p}_3 \tag{6}$$

where $\dot{\ell}$ is the desired velocity of the LOS vector in the payload frame, and $\dot{\ell}$ is the speed of the target relative to the spacecraft along $\boldsymbol{p}_3$. Further, commanded inertial angular velocity of the payload ${}^N\boldsymbol{\omega}_c^P$ in the $\boldsymbol{p}_1, \boldsymbol{p}_2, \boldsymbol{p}_3$ frame equals

$${}^N\boldsymbol{\omega}_c^P = \omega_{p1c}\boldsymbol{p}_1 + \omega_{p2c}\boldsymbol{p}_2 + \omega_{p3c}\boldsymbol{p}_3 \tag{7}$$

Now, since

$$\dot{\boldsymbol{\ell}} = \dot{\ell} + {}^N\boldsymbol{\omega}_c^P \times \boldsymbol{\ell} \tag{8}$$

substituting Eqs. (1), (6), and (7) in Eq. (8), and recognizing that the known inertial velocity $\dot{\boldsymbol{\ell}}$ can be decomposed as

$$\dot{\boldsymbol{\ell}} = \dot{\boldsymbol{\ell}} \cdot \boldsymbol{p}_1 \boldsymbol{p}_1 + \dot{\boldsymbol{\ell}} \cdot \boldsymbol{p}_2 \boldsymbol{p}_2 + \dot{\boldsymbol{\ell}} \cdot \boldsymbol{p}_3 \boldsymbol{p}_3 \tag{9}$$

the ensuing three scalar equations yield the following two inertial rate commands about the $\boldsymbol{p}_1$ and $\boldsymbol{p}_2$ axis:

$$\omega_{p1c} = -(\dot{\boldsymbol{\ell}} \cdot \boldsymbol{p}_2)/\ell \tag{10a}$$

$$\omega_{p2c} = (\dot{\boldsymbol{\ell}} \cdot \boldsymbol{p}_1)/\ell \tag{10b}$$

Since the target must always be collinear with $\boldsymbol{p}_3$, the inertial rate command ω_{p3c} about the $\boldsymbol{p}_3$-axis is arbitrary, and so it can be set equal to the component ω_{p3} of the payload about the $\boldsymbol{p}_3$-axis. Specifically, let ω_{b1}, ω_{b2}, ω_{b3} be the components of the inertial angular velocity $\bar{\boldsymbol{\omega}}_b$ of the base body in the triad $\boldsymbol{b}_1, \boldsymbol{b}_2, \boldsymbol{b}_3$, and let u_{p1c} be the rate command (to be determined momentarily) of the payload about the $\boldsymbol{b}_1$-axis relative to the base body. Then, ω_{p3c} is found to be

$$\omega_{p3c} = \omega_{b1}s\theta_{p2c} - \omega_{b2}s\theta_{p1c}c\theta_{p2c} + \omega_{b3}c\theta_{p1c}c\theta_{p2c} + u_{p1c}s\theta_{p2c} \tag{11}$$

where θ_{p1c} and θ_{p2c} are given by Eq. (4).

If a control system must use position and rate commands simultaneously, then both commands must be either relative or inertial, not mixed. Therefore, since the relative position commands are derived above, it is desirable to know the relative rate commands. Recalling the definition of ω_{b1}, ω_{b2}, and ω_{b3}, the relative rate commands u_{p1c} about the axis

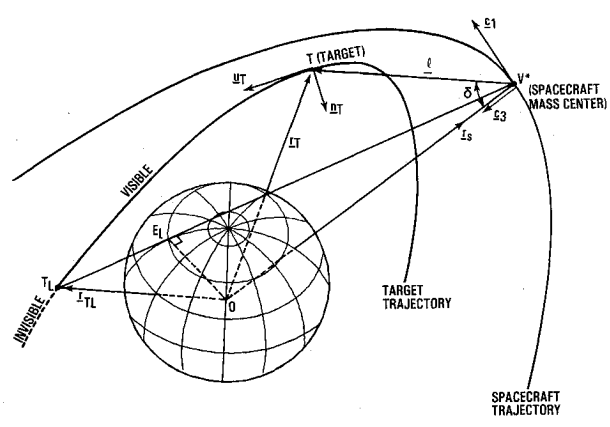

Fig. 2 Spacecraft, target, and the Earth: relative locations.

$\boldsymbol{b}_1(u_{p1c} \triangleq \dot{\theta}_{p1c})$ and u_{p2c} about the axis $\boldsymbol{p}_2(u_{p2c} = \dot{\theta}_{p2c})$ are found to be

$$u_{p1c} = [\omega_{p1c} - (\omega_{b1}c\theta_{p2c} + \omega_{b2}s\theta_{p1c}s\theta_{p2c} - \omega_{b3}c\theta_{p1c}s\theta_{p2c})]/c\theta_{p2c} \tag{12a}$$

$$u_{p2c} = [\omega_{p2c} - (\omega_{b2}c\theta_{p1c} + \omega_{b3}s\theta_{p1c})] \tag{12b}$$

Inertial and Relative Acceleration Commands

As shown in Fig. 2, let $\boldsymbol{u}_T$ and $\boldsymbol{n}_T$ be the instantaneous tangent and normal unit vectors of the target's trajectory, $\boldsymbol{u}_T$ in the direction of the velocity and $\boldsymbol{n}_T$ normal to it. Additionally, let v_T be the instantaneous speed of the target ($\dot{\boldsymbol{r}}_T = v_T\boldsymbol{u}_T$), and ρ_T the instantaneous radius of curvature of the target's trajectory. Then, the inertial acceleration of the target is

$$\ddot{\boldsymbol{r}}_T = (v_T^2/\rho_T)\boldsymbol{n}_T + \dot{v}_T\boldsymbol{u}_T \tag{13}$$

The inertial acceleration of the mass center V^* of the spacecraft $\ddot{\boldsymbol{r}}_s$ is given analogously. The inertial acceleration of the LOS vector $\ddot{\boldsymbol{\ell}}$ is then

$$\ddot{\boldsymbol{\ell}} = \ddot{\boldsymbol{r}}_T - \ddot{\boldsymbol{r}}_s \tag{14}$$

Since the trajectories of the target and the spacecraft are known, $\ddot{\boldsymbol{\ell}}$ is known, and it can be written in the payload frame as

$$\ddot{\boldsymbol{\ell}} = \ddot{\boldsymbol{\ell}} \cdot \boldsymbol{p}_1\boldsymbol{p}_1 + \ddot{\boldsymbol{\ell}} \cdot \boldsymbol{p}_2\boldsymbol{p}_2 + \ddot{\boldsymbol{\ell}} \cdot \boldsymbol{p}_3\boldsymbol{p}_3 \tag{15}$$

On the other hand, by differentiating $\dot{\boldsymbol{\ell}}$ from Eq. (8), utilizing Eqs. (1), (6), and (7), and comparing the resulting expression with Eq. (15), the following inertial acceleration commands about the axes $\boldsymbol{p}_1$ and $\boldsymbol{p}_2$ are secured:

$$\dot{\omega}_{p1c} = -(\ddot{\boldsymbol{\ell}} \cdot \boldsymbol{p}_2 + 2\dot{\ell}\omega_{p1c})/\ell + \omega_{p2c}\omega_{p3c} \tag{16a}$$

$$\dot{\omega}_{p2c} = (\ddot{\boldsymbol{\ell}} \cdot \boldsymbol{p}_1 - 2\dot{\ell}\omega_{p2c})/\ell - \omega_{p1c}\omega_{p3c} \tag{16b}$$

where ω_{p1c}, ω_{p2c}, and ω_{p3c} are obtained from Eqs. (10) and (11). Meanwhile, the relative acceleration commands $\dot{u}_{p1c}$ and $\dot{u}_{p2c}$ are deduced to be

$$\dot{u}_{p1c} = \{\dot{\omega}_{p1c} - [\dot{\boldsymbol{\omega}}_b \cdot \boldsymbol{p}_1 + u_{p1c}s\theta_{p2c}(\boldsymbol{\omega}_b \cdot \boldsymbol{p}_2 - u_{p2c}) - u_{p2c}\boldsymbol{\omega}_b \cdot \boldsymbol{p}_3]\}/c\theta_{p2c} \tag{17a}$$

$$\dot{u}_{p2c} = \dot{\omega}_{p2c} - [\dot{\boldsymbol{\omega}}_b \cdot \boldsymbol{p}_2 + u_{p1c}(\boldsymbol{\omega}_b \cdot \boldsymbol{p}_3c\theta_{p2c} - \boldsymbol{\omega}_b \cdot \boldsymbol{p}_1s\theta_{p2c})] \tag{17b}$$

where $\dot{\boldsymbol{\omega}}_b$ is the attitude acceleration of the base body.

Because of the Earth's finite dimensions, a target is not always visible from the spacecraft. Certain conditions must be satisfied for it to be so. These are formulated in Ref. 8.

III. Pointing Control System

A pointing control system must perform three functions: 1) slew the telescope to acquire the object, 2) settle on that object, and 3) track it precisely. The control system presented here becomes progressively more complex as it proceeds from the third function to the second, and then to the first. Therefore, we will first describe the simplest controller, called a rate mode controller, which is used for precision tracking. It is so named because in this mode it uses rate commands only. Next, we will describe a position mode controller for settling on a moving object; its name stems from its characteristic of using position commands only, no rate commands. The rate mode controller remains as an inner loop of the position mode controller. Finally, to use the position mode controller also for acquiring an object, limits are imposed on the position error, rate, and acceleration of the telescope so that if the limits are exceeded, the telescope will coast to the target. Since the designs are based on a linear, single-axis analysis, the two axes of the telescope will not be distinguished in this section.

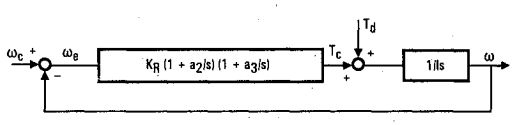

Fig. 3 Rate mode controller for precision tracking.

Rate Mode Controller for Tracking

This controller is shown in Fig. 3; ω_c, ω, and ω_e are the rate command, rate, and rate error. From a single-axis viewpoint, there is no distinction between inertial and relative rates. However, when this controller is used for the payload in Fig. 1, ω_c will represent an inertial rate command. In Fig. 3, T_c and T_d are control and disturbance torques, and I is the moment of inertia of the payload about the axis under consideration. From Fig. 3

$$\omega_e = \omega_c/(1 + G_R) - T_d/[Is(1 + G_R)] \tag{18}$$

where

$$G_R = K'_R(s + a_2)(s + a_3)/s^3, \qquad K'_R = K_R/I \tag{19}$$

and s is the Laplace variable. The parameters K'_R, a_2, and a_3 are > 0. The closed-loop characteristic polynomial of the controller is

$$s^3 + K'_R(s + a_2)(s + a_3) = 0 \tag{20}$$

This control system is a type 3 system (cf. Masten[6]) so that with $T_d = 0$ and the rate command

$$\omega_c(t) = (\omega_{c0} + \dot{\omega}_{c0}t + \ddot{\omega}_{c0}t^2/2)U_{-1}(t) \tag{21}$$

the steady-state rate error $\omega_{e\infty}$ is zero. In Eq. (25), $U_{-1}(t)$ is a step function. Note that if, for example, $a_2 = 0$, $\omega_{e\infty}$ will become $\ddot{\omega}_{c0}/K'_Ra_3$, which indicates the advantage of having both a_2 and a_3 nonzero. On the other hand, the steady-state position error $\theta_{e\infty}$ is ($\dot{\theta}_e \triangleq \omega_e$ for single-axis analysis)

$$\theta_{e\infty} = \ddot{\omega}_{c0}/(K'_Ra_2a_3) + \theta_{e0} \tag{22}$$

where θ_{e0} equals the position error at the instant of switching to the rate mode controller. Regarding the errors caused by the disturbance torque T_d, if T_d represents coloumb friction, then both $\omega_{e\infty}$ and $\theta_{e\infty}$ are zero.

To determine K'_R, a_2, and a_3, express the characteristic equation (20) as

$$(s + \alpha_R)(s^2 + 2\zeta_R\omega_Rs + \omega_R^2) = 0 \tag{23}$$

Now, compare it with Eq. (20) and obtain

$$K'_R = \alpha_R + 2\zeta_R\omega_R \tag{24a}$$

$$K'_R(a_2 + a_3) = \alpha_R \cdot 2\zeta_R\omega_R + \omega_R^2 \tag{24b}$$

$$K'_Ra_2a_3 = \alpha_R\omega_R^2 \tag{24c}$$

Since the objective of the rate mode controller is precision tracking, its bandwidth ω_{BW} and so ω_R would be relatively high. (In the example considered in Sec. V, $\omega_{BW} = 10$ rad/s and $\omega_R = 5$ rad/s.) It is, therefore, desirable that the two real zeros [$-a_2$ and $-a_3$ in Eq. (19)] flank the pair of the complex conjugate poles. Furthermore, to achieve a dominant-pole closed-loop response, the real pole $-\alpha_R$ should be close to the zero that is nearer to the origin. Denoting this zero by $-a_3$,

one has $\alpha_R \approx a_3$. With this reasoning, Eq. (24) leads to

$$K'_R \approx 2\zeta_R\omega_R \tag{25a}$$

$$a_2 = \omega_R/2\zeta_R \tag{25b}$$

$$a_3 \approx \alpha_R \tag{25c}$$

If, on the other hand, instead of $\alpha_R \approx a_3$, one takes $\alpha_R = n\zeta_R\omega_R$, $n < 1$, then by solving Eq. (24) for K'_R, a_2, a_3, one obtains

$$K'_R = (n+2)\zeta_R\omega_R \tag{26a}$$

$$a_2 = 2n\zeta_R\omega_R/(2n\zeta_R^2 + 1 \pm \{1 - 4n\zeta_R^2[1 + n(1-\zeta_R^2)]\}^{\frac{1}{2}}) \tag{26b}$$

$$a_3 = n\omega_R^2/a_2(n+2) \tag{26c}$$

The sign ambiguity in a_2 in Eq. (26) is resolved by requiring that the zeros $-a_2$ and $-a_3$ be astride the complex conjugate poles. After specifying ζ_R, ω_R, and α_R, the parameters K'_R, a_2, a_3 are determined by employing Eq. (25) or Eq. (26). One may also specify the settling time τ_R and determine the product $\zeta_R\omega_R$ according to the relationship $\tau_R = 4/\zeta_R\omega_R$ for settling the rate error to 1% of its initial value. The time τ_R for settling the rate error would be in the range of 1 to 2 s and is considerably smaller than the time required to settle the telescope on a target just after acquisition. The rate mode controller cannot be used for this purpose because, according to Eq. (22), it cannot eliminate any initial position error, its bandwidth ω_{BW} and the frequency ω_R are relatively high, and the damping coefficient ζ_R is relatively small, which will cause the payload to oscillate at a high frequency.

Position Mode Controller for Settling

This controller comprises the rate mode controller as an inner loop, and an outer loop that determines the position error $\theta_e = \theta_c - \theta$ where θ_c equals attitude command (see Fig. 4). The position error is passed through a PI controller $K_P(s + a_1)/s$ to produce a quasirate ω_p of the telescope which, when compared with ω, generates a quasirate error ω_{pe}; ω_{pe} passes through the rate mode controller as ω_e did before.

From Fig. 4, the following relationships can be derived:

$$\theta_e = \theta_c/(1 + G_p) - T_d/[Is^2(1 + G_p)(1 + G_R)] \tag{27}$$

where

$$G_P = \frac{G_R}{1+G_R}\frac{K_P(s+a_1)}{s^2} = \frac{K_PK'_R(s+a_1)(s+a_2)(s+a_3)}{s^2[s^3 + K'_R(s+a_2)(s+a_3)]} \tag{28}$$

The closed-loop characteristic polynomial is found to be

$$s^5 + K'_Rs^2(s+a_2)(s+a_3) + K'_RK_P(s+a_1)(s+a_2)(s+a_3) = 0 \tag{29}$$

This is a type 2 control system. To determine the steady-state error $\theta_{e\infty}$, assume the position command to be

$$\theta_c(t) = (\theta_{c0} + \dot\theta_{c0}t + \ddot\theta_{c0}t^2/2)U_{-1}(t) \tag{30}$$

for which $\theta_{e\infty} = \ddot\theta_{c0}/K_Pa_1$ when $T_d = 0$. If T_d is assumed to be a step torque, then $\theta_{e\infty}$, caused by T_d alone, equals zero.

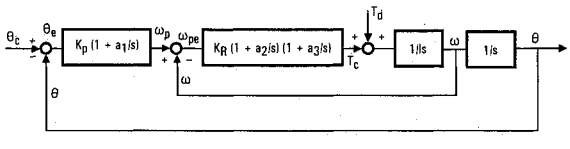

Fig. 4 Position mode controller for settling on a target.

To determine the parameters K_P and a_1, the approximation of the dominant complex pole is used again. First, the closed-loop characteristic polynomial, Eq. (29), is written as

$$(s + \tilde\alpha_R)(s^2 + 2\tilde\zeta_R\tilde\omega_Rs + \tilde\omega_R^2)(s^2 + 2\zeta_p\omega_ps + \omega_p^2) = 0 \tag{31}$$

where $\tilde\alpha_R$, $\tilde\zeta_R$, and $\tilde\omega_R$ are the perturbed values of α_R, ζ_R, and ω_R; ζ_p and ω_p are the damping coefficient and frequency of the dominant complex poles of the position mode. To arrive at the first trial value of a_1, we assume that α_R, ζ_R, and ω_R are not perturbed and specify ζ_p and ω_p according to the desired settling time $\tau_p = 4/\zeta_p\omega_p$, where τ_p may be an order of magnitude longer than τ_R and $\zeta_P \approx 0.71$. Note that the relationship $\tau_p = 4/\zeta_p\omega_p$ is valid for decreasing any magnitude of the initial position error (within linear range) to its 1% value. In precision pointing, however, the actual settling time is the time required to decrease the error to a fixed small value (say 10 arcsec), and so the actual settling time in the position mode varies significantly, for it is governed by the initial angular position, velocity, and acceleration of the telescope. This variation is determined in the next paragraph. Returning to the determination of a_1, it is taken to be equal to $\zeta_p\omega_p$ so that the transients caused by the dominant pole $-\zeta_p\omega_p \pm j\omega_P\sqrt{1-\zeta_p^2}$ ($j^2 = -1$) are smaller than those without a_1. Regarding K_p, recall that for a unity feedback in type 1 or a higher system, when the input is a step function, the steady-state error is zero [Ref. 9, p. 335, Eq. (10.11)]. Accordingly, for a step command $\theta_c(t)$, Eq. (31) yields

$$K_PK'_R \approx \tilde\alpha_R\tilde\omega_R^2\omega_p^2/a_1a_2a_3 \tag{32}$$

which determines K_p because all the other parameters are known.

For an exact determination of the settling times for a variety of initial conditions, the theory of complex residues can be employed. For simplicity, however, we maintain the assumption that the rate mode poles are not perturbed by the position mode and further assume that $T_d = 0$ in Eq. (27). Then, θ_e is found to be related to the initial conditions θ_{c0}, $\dot\theta_{c0}$, and $\ddot\theta_{c0}$, thus

$$\theta_e(t) = \ddot\theta_{c0}/\omega_p^2 + e^{-\zeta_p\omega_pt}\gamma\sin(\omega_p\sqrt{1-\zeta_p^2}\,t + \phi) \tag{33}$$

where

$$\gamma^2 = \gamma_1^2 + \gamma_2^2 + 2\gamma_1\gamma_2\cos(\phi_1 - \phi_2), \qquad \phi = \tan^{-1}\frac{\gamma_1s\phi_1 + \gamma_2s\phi_2}{\gamma_1c\phi_1 + \gamma_2c\phi_2}$$

$$\gamma_1 = [(\dot\theta_{c0} - a\theta_{c0})^2 + (\theta_{c0}b)^2]^{1/2}/b, \qquad \gamma_2 = -\ddot\theta_{c0}/\omega_p^2\sqrt{1-\zeta_p^2}$$

$$\phi_1 = \tan^{-1}[b/(\dot\theta_{c0}/\theta_{c0} - a)],$$

$$\phi_2 = \cos^{-1}\zeta_p, \qquad a = \zeta_p\omega_p, \qquad b = \omega_p\sqrt{1-\zeta_p^2} \tag{34}$$

Now, the settling time required to decrease the pointing error to a specified value of $\theta_e(t)$, say 10 arcsec, can be determined easily.

Nonlinear Control System

When the position error between the telescope and the target exceeds a certain limit (say $\pm n_\theta$), or when the inertial rate of the telescope about either of its two axes crosses a certain bound (say $\pm n_\omega$), or when the desired control torque outstrips the capacity of the electric motor onboard, then the telescope may simply be coasted toward the target. To do so, certain limiters must be introduced in the position mode controller of Fig. 4. This nonlinear control system is shown in Fig. 5 where, instead of showing a limit on the control torque, a limit on the telescope's acceleration $\pm n_\alpha$ is shown. The limits n_θ and n_ω are related as $n_\omega = K_Pn_\theta$.

IV. Steady-State Errors in the Case of Arbitrary Commands

It is assumed in Sec. III that the position and rate commands are, at the most, parabolic. However, the commands for a moving target varies much more and, therefore, for precision pointing, the frequency spectrum of the actual command and the steady-state error in following it with a given control system must be determined. The telescope observes a target for a brief interval, and so there are two approaches to determine the frequency spectrum: the command may be taken as periodic with a period equal to the observation interval, or aperiodic, existing only for the observation interval. Clearly, the latter approach, which generates a continuous spectrum, is closer to reality than the former, which leads to a discrete spectrum. However, the steady-state error analysis for a command with a discrete spectrum is relatively simple and is adequate for the present purposes. Consequently, this is considered in the next section. For the error analysis for a command with continuous spectrum, see Ref. 8.

Steady-State Error for a Periodic Rate Command

The rate command, Eq. (10), can be expanded as the following periodic function:

$$\omega_c(t) = \bar{\omega}_c + \bar{\alpha}_c(t - T/2) + \sum_{k=\pm1,\pm2,\ldots} A_k e^{j\omega_k t}$$

$$\omega_k = 2\pi f_k, \qquad 0 \le t \le T \tag{35}$$

where an overbar indicates the mean of that variable, $\bar{\alpha}_c$ = mean acceleration command, A_k = complex amplitude of the kth harmonic having the frequency f_k, $f_k = k/T$. In Eq. (35), $\omega_c(t)$ is periodic, bounded, and exists for all time $-\infty \le t \le \infty$, whereas in Eq. (21), $\omega_c(t)$ exists only for $0 \le t \le \infty$ and as $t \to \infty$, $\omega_c(t) \to \infty$.

To determine the spectral density of the periodic command $\omega_c(t)$, define the finite Fourier transform and the finite delta functions $\delta_0(f)$ and $\delta_k(f)(k = \pm1, \pm2,\ldots)$ as did Bendat and Piersol[10] (Sec. 1.2.3). The one-sided discrete spectral density of ω_c then equals (Ref. 10, Sec. 4.1.3)

$$P_{\omega c} = 2[\bar{\alpha}_c^2/\omega_k^2 + A_k A_k^* + 2A_{kI}\bar{\alpha}_c/\omega_k]\delta_k(f) + 2\bar{\omega}_c^2\delta_0(f)$$

$$(k = 1,2,\ldots) \tag{36}$$

where A_k^* = the complex conjugate of A_k, and A_{kI} = the imaginary part of A_k.

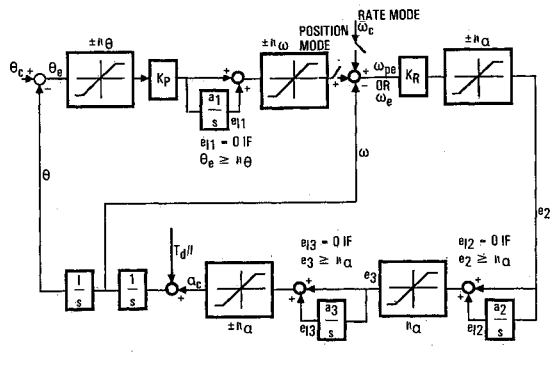

Fig. 5 Nonlinear controller for acquiring and tracking a moving object.

To evaluate the steady-state mean square rate error $\omega_{e\infty}^2$, recall Eq. (18), keep $T_d = 0$, and substitute the definition $H_R(s) \triangleq 1/[1 + G_R(s)]$, which yields

$$|H_R(\omega)|^2 = \omega^6/\{(\omega^2 + \alpha_R^2)[(-\omega^2 + \omega_R^2)^2 + 4\omega^2\zeta_R^2\omega_R^2]\} \tag{37}$$

The mean $\bar{\omega}_e$ in response to the nonzero $\bar{\omega}_c$ will be zero because $H_R(0) = 0$ and $\bar{\omega}_e = H_R(0)\omega_c$. The mean square rate error then equals

$$\omega_{e\infty}^2 = 4\sum_k |H_R(\omega_k)|^2[\bar{\alpha}_c^2/\omega_k^2 + A_k A_k^* + 2A_{kI}\bar{\alpha}_c/\omega_k] \tag{38}$$

Steady-State Error for a Periodic Position Command

A periodic position command $\theta_c(t)$ can be written as

$$\theta_c(t) = \bar{\theta}_c + \bar{\theta}_c(t - T/2) + \bar{\bar{\theta}}_c(t^2/2 - Tt/2 + T^2/12) + \sum_{k=\pm1,\pm2,\ldots} B_k e^{j\omega_k t}, \qquad 0 \le t \le T \tag{39}$$

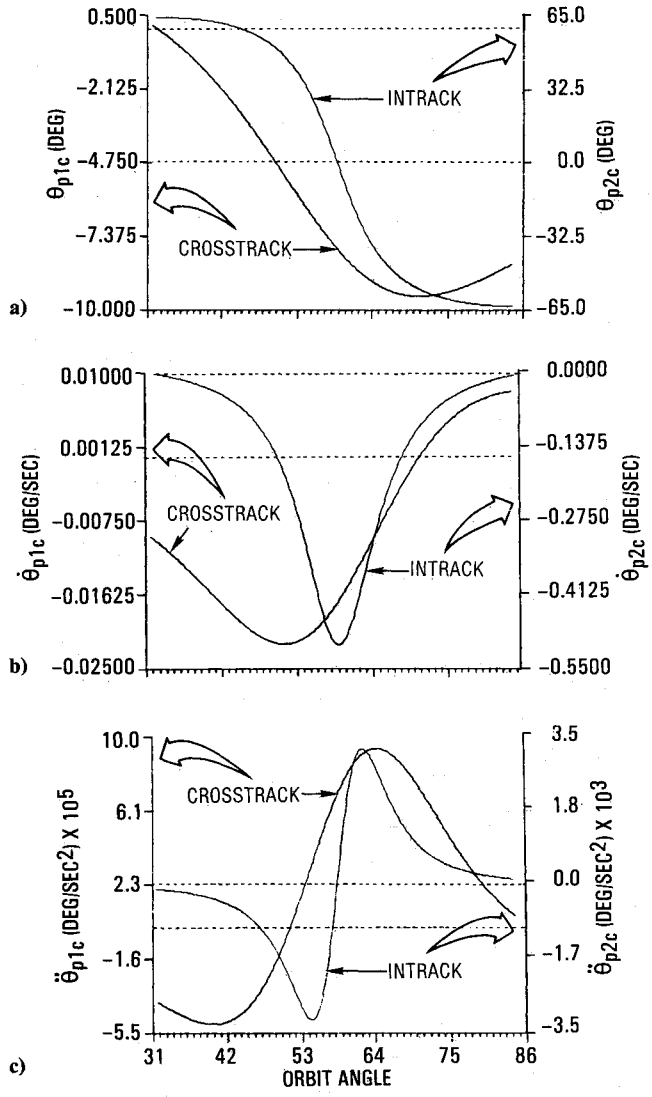

Fig. 6 Relative position, rate, and acceleration command profiles for landmark observation.

Next, define $H_p(s) \triangleq 1/[1 + G_p(s)]$, so that from Eq. (31)

$$|H_p(\omega)|^2 = \frac{\omega^4(\alpha_R^2 + \omega^2)[(\omega_R^2 - \omega^2)^2 + (2\zeta_R\omega_R\omega)^2]}{(\tilde{\alpha}_R^2 + \omega^2)[(\tilde{\omega}_R^2 - \omega^2)^2 + (2\tilde{\zeta}_R\tilde{\omega}_R\omega)^2][(\omega_p^2 - \omega^2)^2 + (2\zeta_p\omega_p\omega)^2]} \tag{40}$$

The mean square steady-state position error $\theta_{e\infty}^2$ is then found to be

$$\theta_{e\infty}^2 = 2 \sum_{k=1,2,\ldots} |H_p(\omega_k)|^2[(\bar{\theta}_c/\omega_k)^2 + (\bar{\dot{\theta}}_c/\omega_k^2 + B_k) \times (\bar{\dot{\theta}}_c/\omega_k^2 + B_k^*) + 2B_{kI}\bar{\dot{\theta}}_c/\omega_k] \tag{41}$$

where B_k^* = the complex conjugate of B_k, and B_{kI} = the imaginary part of B_k. Eq. (41) may be compared with Eq. (38).

V. Numerical Results and Discussion

Command Profiles

The command equations of Sec. II are illustrated here for terrestrial observations. Assume that the spacecraft shown in Fig. 1 traverses a 100-min circular orbit, and its telescope tracks a landmark that moves because of the Earth's rotation. Figure 6 shows the relative position, rate, and acceleration command profiles for the telescope about the cross-track axis $\boldsymbol{b}_1$ and the in-track axis $\boldsymbol{p}_2$. The commands are relative to the base body that rotates ideally once per orbit. The landmark and spacecraft's orbital parameters to obtain these profiles are recorded in Ref. 8. The profiles are shown for one horizon-to-horizon duration. In the cross track, the payload moves at the most by 10 deg at a maximum rate of 0.022 deg/s and acceleration 9×10^{-5} deg/s^2; in the in-track, the payload sweeps a wide arc of 130 deg with a maximum rate of 0.5 deg/s when the landmark is directly beneath the payload, and a maximum acceleration of 0.0032 deg/s^2. Clearly, the relative motion of the landmark is mostly in the orbital plane. The mean $\bar{\theta}_c$ and $\bar{\dot{\theta}}_c$ of these profiles are furnished in Ref. 8.

Since the frequency spectrum of a command profile and error specifications give a reliable estimate of the bandwidth of a control system that will follow that profile, the frequency spectrum of the rate profiles in Fig. 6b is determined now. The horizon-to-horizon interval T equals 876 s, and the command profiles are sampled at a uniform interval of 0.1 s, and so the fundamental frequency $1/T = 1.14E - 3$ Hz, and the maximum frequency, which the spectra can have, is 5.0 Hz. Subtracting the linear term $\bar{\dot{\theta}}_c(t - T/2)$ from the rate profiles, the cosine $\mathcal{C}$ and the sine $\mathcal{S}$ transforms of the residuals, denoted $\dot{\theta}_{p1c}$ and $\dot{\theta}_{p2c}$, are shown in Fig. 7. Observing the in-track rate command $\dot{\theta}_{p2c}$ in Fig. 6b, one gathers that its cosine harmonics predominate over sine harmonics. Precisely this is seen in Fig. 7. On the other hand, $\dot{\theta}_{p1c}$ in Fig. 6b and its transforms in Fig. 7 exhibit no such feature. Since the in-track rate commands are about an order of magnitude larger than the cross-track rate commands, the corresponding transforms in Fig. 7 also exhibit that sort of ratio; the ratio is one to three orders of magnitude in the low-frequency regime, and it gradually diminishes as the frequency approaches 5.0 Hz. The frequencies up to which the sine and cosine harmonics of the transforms of the commands must be retained in order for the truncation errors in the expansion, Eq. (35), to be no greater than 1 arcsec/s for the entire duration are: in cross track, 0.00915 Hz (i.e., up to $k = \pm 8$), and in in-track, 0.047 Hz (i.e., up to $k = \pm 41$). The time history of both the errors is shown in Fig. 8.

The command profiles exhibited in Fig. 6 do not include base body motion caused by disturbance torques. On the other hand, to keep the solar array of the spacecraft sun-oriented, the solar array is driven by a periodic, pulsating torque at a frequency of 0.078 Hz. This torque excites transverse and in-plane bending of the solar array at the frequencies 0.51 and 1.31 Hz and torsion at 2.33 Hz; these modes in turn disturb the base body attitude at the above frequencies. To determine inertial rate commands for the telescope, the attitude angles and rates of the base body are employed; therefore, the above modal frequencies manifest themselves in the real rate commands. The frequency limits 0.009 and 0.047 Hz, determined in the previous paragraph, are tentative, and a controller's bandwidth is, empirically, about 10 times these limits. However, keeping in mind the solar array controller torque frequency 0.078 Hz and the flexibility considerations, the bandwidth ω_{BW} of the rate mode controller for both axes may be set at 1.6 Hz (20×0.078 or 34×0.047). This selection ineluctably generates some control-structure interaction, which is evaluated in Ref. 11. Regarding the position mode controller, owing to settling time considerations, its bandwidth is set at ~ 0.3 Hz.

Root Loci and Bode Plots

For the rate mode controller, the specifications are:

$$\tau_R = 1.5 - 1.75 \text{ s}, \qquad \text{per unit overshoot} = 20\%$$
$$\omega_R = 0.75 - 0.80 \text{ Hz}, \qquad n[\text{Eq. (26)}] = 0.50 \tag{42}$$

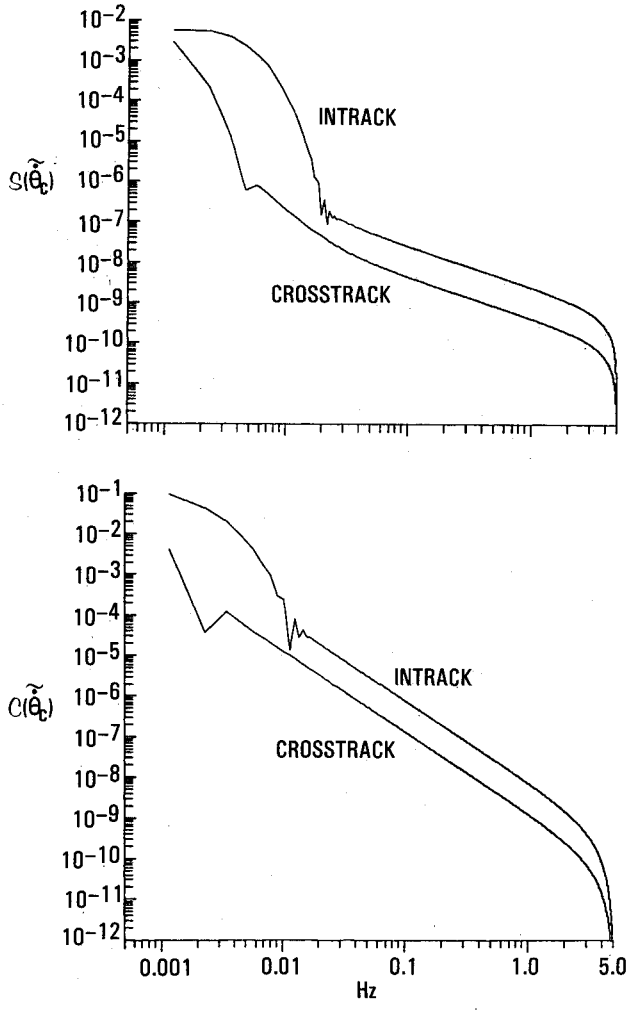

Fig. 7 Sine and cosine transforms of the residual cross-track and in-track rate commands.

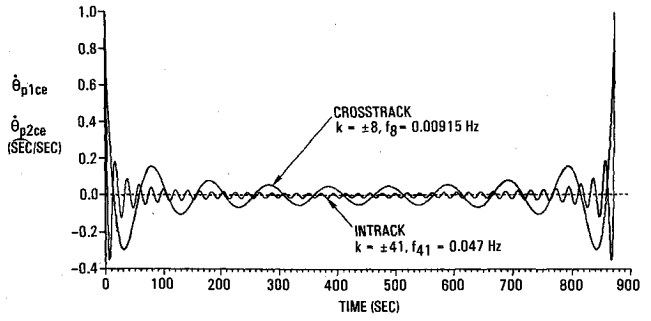

Fig. 8 Errors in truncating rate command profiles.

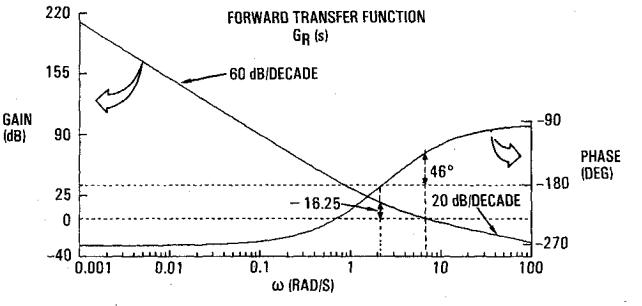

Fig. 10 Bode plot of the rate mode controller.

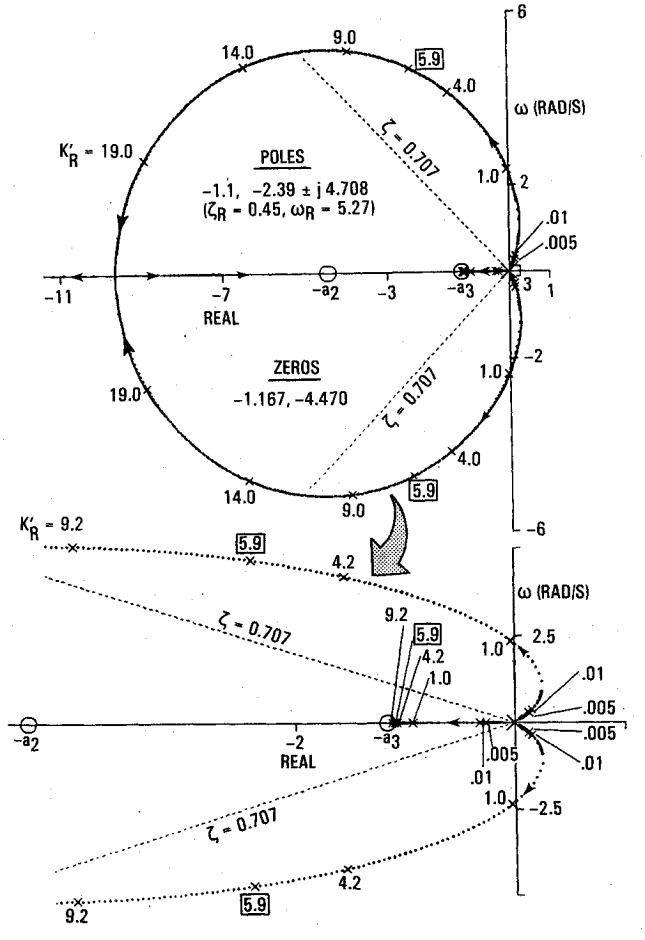

Fig. 9 Root locus of the rate mode controller.

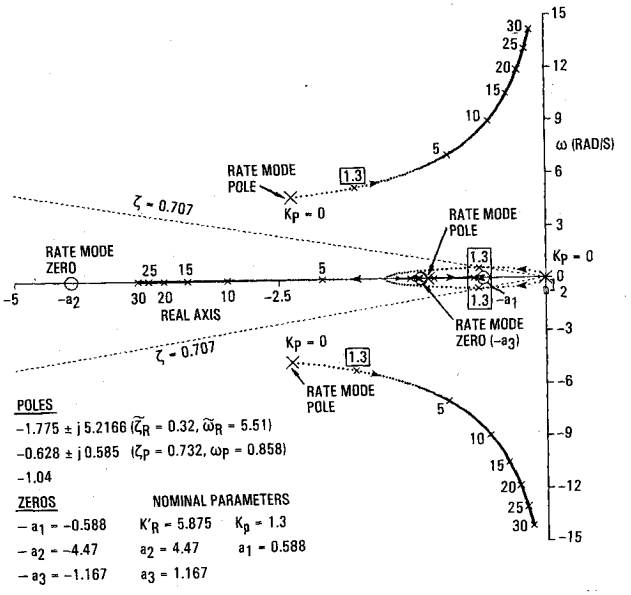

Fig. 11 Root locus of the position mode controller.

and to satisfy these specifications, the parameters are set at [Eq. (26)]: $K'_R \approx 5.9$, $a_2 \approx 4.5$, and $a_3 \approx 1.17$. A root locus diagram obtained by varying K'_R is shown in Fig. 9. This type 3 system is unstable for $K'_R < 1.0$. The operating point $K'_R = 5.9$ is on a sufficiently flat portion of the root locus, so that the controller is insensitive to parametric variations. The poles and zeros corresponding to the nominal parameters above are recorded in the top part of Fig. 9. The negative real pole (-1.1) and the zero (-1.167) are very close to each other, and the dynamic response is essentially controlled by the pair of the complex conjugate poles that has $\omega_R = 0.84$ Hz and $\zeta_R = 0.45$. The zero $-a_2$ is sufficiently left of the dominant complex pole. A Bode plot of the forward transfer functions G_R is shown in Fig. 10. Since this is a type 3 system, it has a low-frequency gain margin of -16.25 dB at the frequency 2.1 rad/s, and infinite high-frequency gain margin. Further, the system has a phase margin of 46 deg at the crossover frequency, 6.8 rad/s. From the Bode plot of the overall transfer function,[8] the second-order dynamics of the system at the frequency ω_R and the system's bandwidth of 10 rad/s (1.6 Hz) are apparent.

Next, consider the position mode controller. We stipulate for

$$\tau_p = 7 \text{ s}, \qquad \text{per unit overshoot} = 4\text{–}5\%,$$

$$\omega_p = 0.125 - 0.150 \text{ Hz} \tag{43}$$

which, after some iterations, yield $K_p = 1.3$ and $a_1 = 0.59$. The parameters K'_R, a_2, a_3 are not disturbed. The root locus drawn by varying K_p is shown in Fig. 11 where the original rate mode poles and zeros (for $K_p = 0$) are also identified. With $K_p = 1.3$, the complex pair of the rate mode poles has moved slightly, whereas the real rate mode pole has moved negligibly. The pair of the low-frequency complex conjugate poles $(-0.628 \pm j0.585)$ for which $\zeta_p = 0.73$, $\omega_p = 0.14$ Hz, and the real zero -0.59, both responsible for settling the payload on a landmark, are also shown in Fig. 11. The relative locations of the closed-loop poles and zeros for nominal parameters signify that the dominant pole approximation is valid. A Bode plot of $G_p(s)$ is portrayed in Fig. 12. Since the phase plot of $G_p(s)$ reaches 180 deg asymptotically, the high-frequency gain margin is theoretically infinite. The phase margin is 65 deg at the crossover frequency, 1.4 rad/s (0.22 Hz). From the Bode plot of $G_p/(1+G_p)$[8] the bandwidth is 2 rad/s (0.32 Hz), whereas the frequency of the maximum gain is ~0.7 rad/s (0.11 Hz).

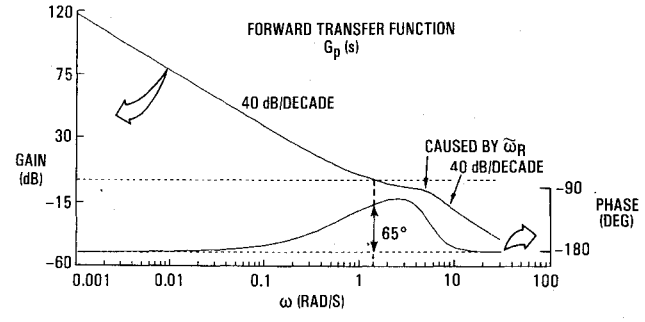

Fig. 12 Bode plot of the position mode controller.

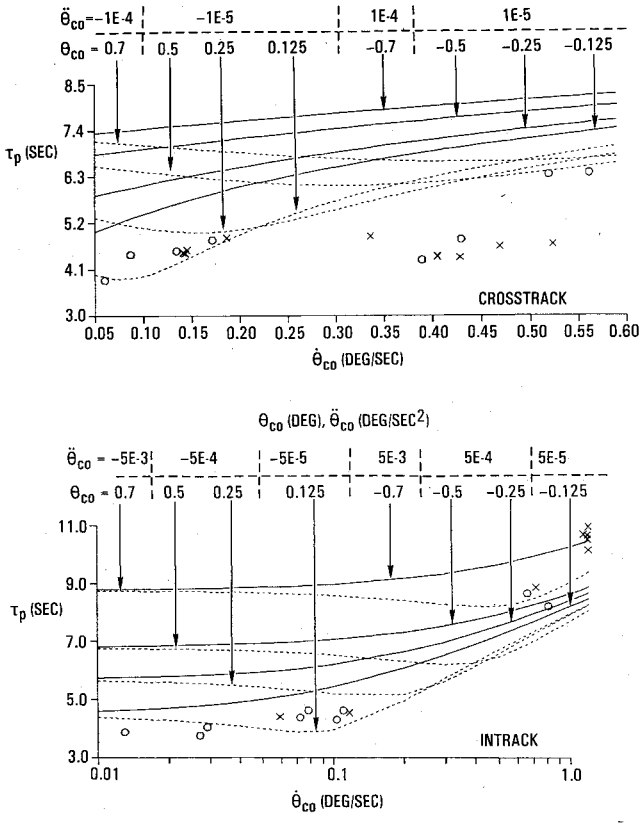

Fig. 13 In-track and cross-track settling times.

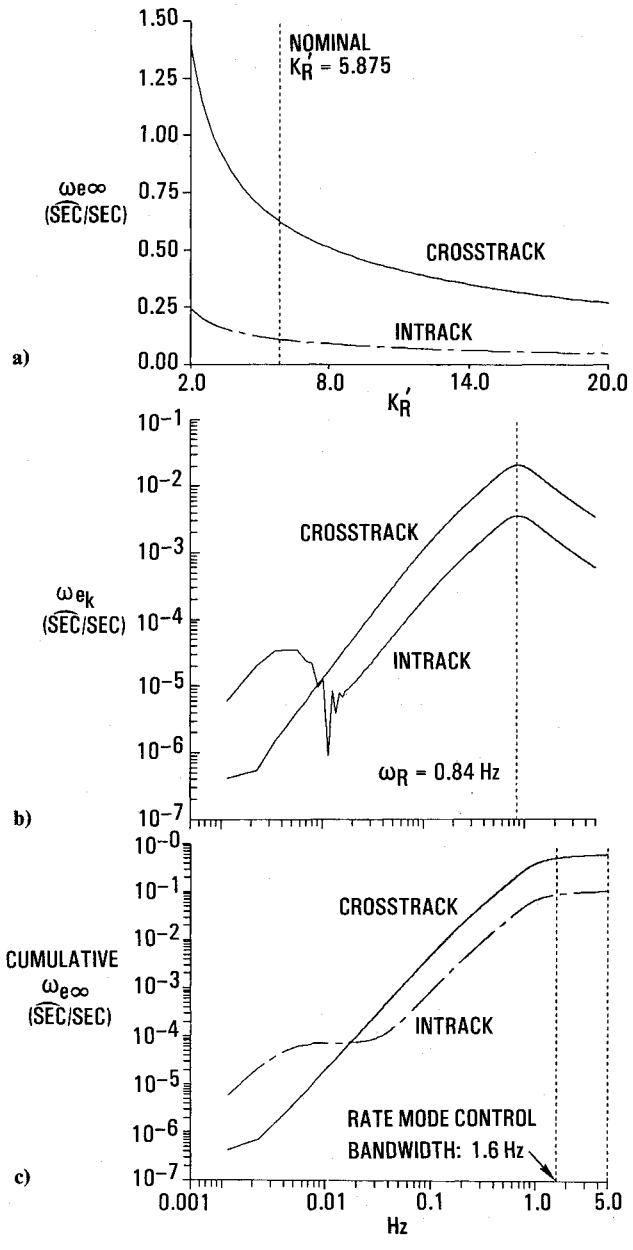

Fig. 14 a) $\omega_{e\infty}$ vs K'_R, b) $\omega_{e\infty}$ caused by each harmonic in the Fourier transform, and c) growth patterns of $\omega_{e\infty}$ as each harmonic is successively added.

Settling Times and Steady-State Rate Errors

Refer to Fig. 5; the limits on the position error, angular velocity, and acceleration are set at $n_0 = 0.7$ deg, $n_\omega = 0.9$ deg/s, and $n_\alpha = 0.01$ rad/s^2. When the coasting phase, if any, terminates, the telescope may have a variety of residual errors in position, velocity, and acceleration; and to decrease the position errors to < 40 arcsec and to keep it so for the remaining period of tracking, the required settling time is determined by using the approximate time history of the position error, Eq. (33). For eight initial values of the position command θ_{c0}, which cover the linear range -0.7 to 0.7 deg, the variation of the settling time with $\dot{\theta}_{c0}$ is displayed in Fig. 13. Since a landmark can have an angular velocity as high as ~ 0.5 deg/s in the in-track, the velocity of the telescope relative to the landmark (and so $\dot{\theta}_{c0}$) may reach ~ 1.4 deg/s; in the cross-track the velocity difference will be smaller. Moreover, from Eq.(33), the maximum possible $\ddot{\theta}_{c0}$ for $\theta_e(\tau_p) \leq 40$ arcsec is $\sim 8.18 \times 10^{-3}$ deg/s^2. As seen from Fig. 13, the in-track settling time may range from 3 to 11 s, and the cross-track settling time from 4 to 8 s. The symbols x and o in Fig. 13 are explained below under Multibody Digital Simulation Results.

The variation of the steady-state rate error $\omega_{e\infty}$, Eq. (38), about the cross-track and in-track axes with the gain K'_R, $2 \leq K'_R \leq 20$, is shown in Fig. 14a. Earlier, $K'_R = 5.9$ was selected because it then yields desirable transient and stability properties (Figs. 9 and 10); Fig. 14a lends additional support to this selection because for this value the $\omega_{e\infty}$ curves are just past their knees. Occasionally, the allowable steady-state rate error is specified in the frequency domain. Therefore, for $K'_R = 5.9$, Fig. 14b illustrates the square root of each term of the series in Eq. (38). For the discussion, abbreviate Eq. (38) to $\omega^2_{e\infty} = \Sigma_k \omega^2_{ek}$. In Fig. 14b, ω_{ek} generally increases with frequency until around 0.8 Hz, where the peak of the overall transfer function gain occurs[8]; beyond that frequency, ω_{ek} declines. Figure 14b shows a valley in the $\omega_{ek,IT}$ curve in the low-frequency regime; its cause is traced in Ref. 8. Figure 14c illustrates the growth of $\omega_{e\infty}$ as ω_{ek} are added successively. The errors increase somewhat steadily with frequency and begin to level off near the controller's bandwidth 1.6 Hz.

Multibody Digital Simulation Results

To ascertain that the control system of Sec. III, synthesized on the basis of simplified analysis, will function onboard a multibody flexible spacecraft (Fig. 1) as desired, an extensive digital simulation was developed. In short, the simulation includes three-body flexible dynamics of the spacecraft in the form of vehicle modes with free hinges, a three-axis controller of the base body, a single-axis controller of the solar array, the nonlinear in-track and cross-track controllers (Fig. 5), and the pointing equations (Sec. II). Regarding the maneuvers of the telescope, it may either step away from one target and settle on the next, or it may change the focal plane zone to view a landmark differently. The former maneuver is called a step-and-stare, and the latter a zonal maneuver. Arrived at with the simulation, in Fig. 13 the settling times of the step-and-stare maneuvers are marked x, and those of the zonal maneuvers o. It can be concluded from Fig. 13 that, generally, the simplified analysis predicts surprisingly accurate settling times.

An example of a step-and-stare maneuver that entails observing four landmarks in succession is illustrated in Fig. 15. The history of the relative position command θ_{p2c}, relative position θ_{p2}, and the error $\theta_{p2e} = \theta_{p2c} - \theta_{p2}$ are displayed in Fig. 15a. The coasting, settling, and tracking phases for each landmark are clearly seen in the figure. The inertial in-track rate command ω_{p2c} and the actual rate ω_{p2} during this maneuver are shown in Fig. 15b. Notice that before reaching $\omega_{p2c} \approx -0.55$ deg/s, the telescope reverses its rate from $+0.9$ deg/s to -0.9 deg and then damps it to ω_{p2c}, instead of reaching ω_{p2c} directly. Such a response stems from the lack of rate command in the position mode; consequently, the rate ω_{p2} takes longer to settle on ω_{p2c}. The above extreme reversal will not take place when, for instance, a time-optimal control policy[4] is employed. Indeed, in comparison to the slewing and settling periods of 16.0, 29.5, 29.0, and 29.0 s for the four landmarks with the proposed controller, the time-optimal controller (the limits remaining the same) took 10.6, 21.7, 24.7, and 25.3 s. In Fig. 15c, the position error of the proposed controller is shown at a magnified scale. Figure 16 compares analytical steady-state rate errors (Fig. 14) with the simulation results for rigid and flexible spacecraft. The periodic increments in the rate errors at a period of 12.7 s are caused by the previously discussed interaction between the payload and the solar array control system via the base body. For a rigid spacecraft, the agreement between the simplified analysis and the simulation results is excellent; however, for a flexible spacecraft, the rigid analysis is inadequate.

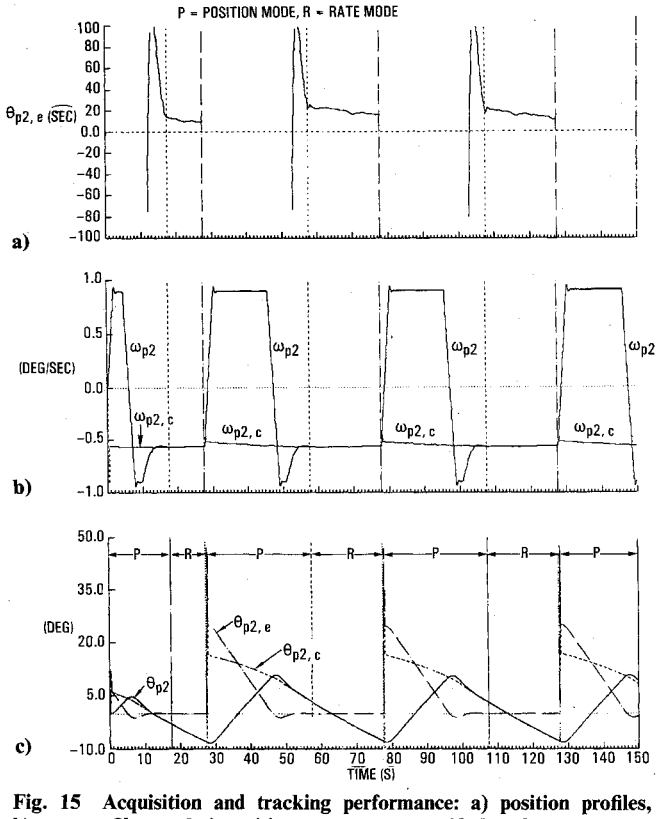

Fig. 15 Acquisition and tracking performance: a) position profiles, b) rate profiles, and c) position error at a magnified scale.

VI. Concluding Remarks

The position, velocity, and acceleration commands derived above for a two-degree-of-freedom telescope articulated to a base body are for arbitrarily moving targets and are useful in a wider context than illustrated here. Although the Fourier spectrum of the commands, idealized by the assumption that the base body is inertially stationary or has a uniform once-per-orbit rotation, does indicate the bandwidth of the required tracking control system, the indication is not adequate. For precise tracking, it is imperative to consider the short-term dynamics of the base body such as that caused by a recurrent solar array controller torque. Classical control theory, with its apparent simplism, can be used successfully to

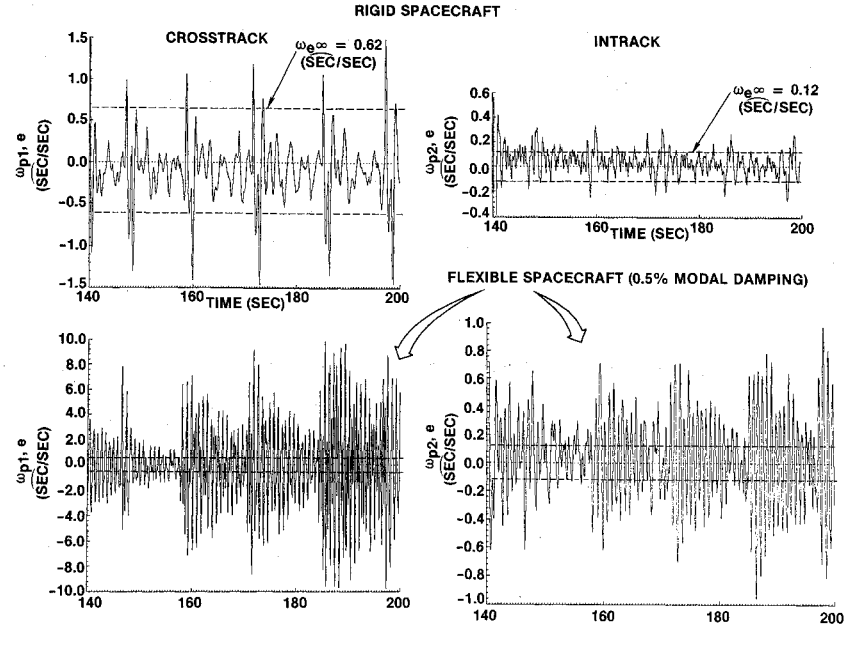

Fig. 16 Steady-state rate errors from digital simulation.

design a precision tracking control system for a typical multibody flexible spacecraft. Indeed, based on single-axis, rigid spacecraft, and dominant pole approximations, the settling times required by a telescope to settle on a moving target can be predicted accurately by classical tools, even though the spacecraft has a flexible solar array and minor interaxial coupling exists. The steady-state error analysis presented in this paper ignores flexibility of the spacecraft; the flexibilty, however, causes significant differences in the analysis and simulation results. It is believed that when flexibility is included, sufficiently accurate results will follow. For a rigid spacecraft, the agreement is excellent. Although attitude, rate, and acceleration commands to track a moving target exist for a finite interval, the assumption that they are periodic with a period equal to the time span during which the target is visible, does yield accurate steady-state error results. This assumption leads to a discrete Fourier spectrum for which error analysis can be performed readily; otherwise, one must contend with sinc function that makes evaluation of integrals in error analysis difficult. Although the proposed controller is illustrated for landmark observation, its parameters can also be determined for other purposes, such as celestial observation, after the performance specifications are decided.

References

[1]Jerkovsky, W., "A Computationally Efficient Pointing Command Law," AIAA Paper 83-2208, Aug. 1983.

[2]Burdick, G. M., Lin, H. S., and Wong, E. C., "A Scheme for Target Tracking and Pointing During Small Celestial Body Encounters," *Journal of Guidance, Control, and Dynamics*, Vol. 7, July–Aug. 1984, pp. 450–457.

[3]Man, G. K. and Breckenridge, W. G., "Command Profile for Galileo Scan Platform Control," AIAA Paper 81-190, Aug. 1981.

[4]Zwartbol, T., Hameetman, G. J., Slippens, C. P. R. C., and Terpsira, A. P., "Experiments in Modern Control On-Board IRAS," *Proceedings of the AIAA Guidance and Control Conference*, AIAA, New York, 1984, pp. 302–315.

[5]Hughes, R. O., "Conceptual Design of Pointing Control Systems for Space Station Gimbaled Payloads," AIAA Paper 86-1986, Aug. 1986.

[6]Masten, M. K., "Application of Control Theory to Design of Line-of-Sight Stabilization Systems," *American Control Conference*, Boston, MA, June 1985, pp. 1219–1222.

[7]Sirlin, S. W. and Bell, C. E., "Soft Mounted Momentum Compensated Pointing System for the Space Shuttle Orbiter," The Society of Photo-Optical Instrumentation Engineers, *Proceedings*, Bellingham, WA, Vol. 641, April 1986, pp. 160–173.

[8]Hablani, H. B., "Design of a Spacecraft Pointing Control System for Tracking Moving Objects," AIAA Paper 87-2597, Aug. 1987.

[9]D'Azzo, J. J. and Houpis, C. H., *Linear Control System Analysis and Design*, McGraw-Hill, New York, 1975.

[10]Bendat, J. S. and Piersol, A. G., *Engineering Applications of Correlation and Spectral Analysis*, Wiley, New York, 1980.

[11]Hablani, H. B, "Evaluation of Image Stability of a Precision Pointing Spacecraft," *Journal of Guidance, Control, and Dynamics*, Vol. 10, May–June 1988, pp. 283–286.